Layer-by-layer and intrinsic analysis of molecular and thermodynamic properties across soft interfaces

Marcello Sega, Balázs Fábián, and Pál Jedlovszky

Articles you may be interested in

Orientational order as the origin of the long-range hydrophobic effect
J. Chem. Phys. **142**, 134505 (2015); 10.1063/1.4916744

Free energy surface of ST2 water near the liquid-liquid phase transition
J. Chem. Phys. **138**, 034505 (2013); 10.1063/1.4775738

Phase stability in nanocrystalline metals: A thermodynamic consideration
J. Appl. Phys. **102**, 124303 (2007); 10.1063/1.2822473

Influence of the cap layer on the Gibbs free energy above a layer of buried InGaAs islands
J. Vac. Sci. Technol. B **20**, 544 (2002); 10.1116/1.1450592

Hard sphere perturbation theory for thermodynamics of soft-sphere model liquid
J. Chem. Phys. **115**, 4766 (2001); 10.1063/1.1392359

Layer-by-layer and intrinsic analysis of molecular and thermodynamic properties across soft interfaces

Marcello Sega,[1] Balázs Fábián,[2,3] and Pál Jedlovszky[4,5,6]

[1]*Computational Physics Group, University of Vienna, Sensengasse 8/9, 1090 Vienna, Austria*
[2]*Institut UTINAM (CNRS UMR 6213), Université de Franche-Comté, 16 route de Gray,*
F-25030 Besançon, France
[3]*Department of Inorganic and Analytical Chemistry, Budapest University of Technology and Economics,*
Szt. Gellért tér 4, H-1111 Budapest, Hungary
[4]*Laboratory of Interfaces and Nanosize Systems, Institute of Chemistry, Eötvös Loránd University,*
Pázmány P. Stny 1/A, H-1117 Budapest, Hungary
[5]*MTA-BME Research Group of Technical Analytical Chemistry, Szt. Gellért tér 4, H-1111 Budapest, Hungary*
[6]*Department of Chemistry, EKF, Leányka u. 6, H-3300 Eger, Hungary*

Interfaces are ubiquitous objects, whose thermodynamic behavior we only recently started to understand at the microscopic detail. Here, we borrow concepts from the techniques of surface identification and intrinsic analysis, to provide a complementary point of view on the density, stress, energy, and free energy distribution across liquid ("soft") interfaces by analyzing the respective contributions coming from successive layers. © 2015 AIP Publishing LLC. [http://dx.doi.org/10.1063/1.4931180]

I. INTRODUCTION

Soft interfaces, the boundary regions between different phases in liquids, gels, membranes, glasses, colloids, and other classes of soft matter, play a key role in many areas of science including cell biology, colloid chemistry, and smart materials. Soft interfaces are the subject of broad scientific investigations thanks to the development of several surface sensitive experimental methods, such as neutron[1] and x-ray reflection,[2] time-dependent fluorescence anisotropy,[3,4] or various nonlinear spectroscopic techniques (like second harmonic and sum frequency generation spectroscopies),[5,6] and also due to the rapid development of the routinely available computing capacity, which allows for an in-depth investigation of interfaces.

By having powerful computers and atomistic level computer simulation methods[7] at hand, the understanding of the thermodynamic behavior of soft interfaces can, in principle, be also done at the molecular level, by calculating the dependence of the various thermodynamic properties (for example, energy, density, and pressure) on the distance from the interface. Such a description requires knowing the exact location of the interface itself.

Soft interfaces are corrugated from the molecular length scale, up to the mesoscopic level, by thermal capillary waves, whose amplitude is characterized by a mild, logarithmic divergence in the long wavelength limit. Thus, when the system is seen at atomistic resolution, such as in computer simulations, the detection of the exact position of the interface is hindered by the presence of these capillary waves. For a while, this problem was simply disregarded, and the interfacial region was defined as that region where the non-intrinsic density profiles (that is, calculated with respect to the simulation box reference frame, also known as global density profiles) are changing from the respective constant values attained far from the interface. From the non-intrinsic density profile, it is not possible

to determine the microscopic location of the interface. Several equivalent options are commonly used to define the so-called Gibbs dividing surface, such as the equimolar one, defined for single component systems as that choice that makes the surface excess density $\rho_s = \rho_{tot} - \rho_{liq}(z_s/L) - \rho_{vap}(1 - z_s/L)$ vanish, where ρ_{liq} and ρ_{vap} are the densities of the two phases (here liquid and vapor) far from interface, z_s, ρ_{tot} is the total density, and z_s/L is the relative extension of the liquid phase. Another common choice is to define the interface at the location where the density of one component equals the average value in the two phases far from the interface.

These approaches are obviously not suited for a microscopic investigation of the interfacial properties. To remove the problem raised by the presence of capillary waves, one has to either identify the full set of molecules that are located at the interface or detect the exact location of the real, capillary wave corrugated, so-called intrinsic interface. Once one of these two tasks is accomplished, the other one can easily be done.

In their pioneering work, Chacón and Tarazona described a procedure, called intrinsic sampling method, to locate the intrinsic surface of a given fluid phase as a surface of minimum area covering a set of pivot atoms. The set of these pivot atoms is determined in a self-consistent iterative process.[8] Another approach is based on dividing the simulation box into several slabs parallel with the surface normal axis and locating the position of the interface in each slab separately.[9,10] Jorge and Cordeiro determined the number of slabs needed to attain a convergent result.[11] Chowdhary and Ladanyi determined the set of surface molecules at the interface of two condensed fluid phases using a criterion based on the vicinity of the molecules of the opposite phase.[12] The extension of this method, by the introduction of a scalable parameter, was shown to give compatible results with the above two approaches.[13] The Identification of the Truly Interfacial Molecules (ITIM) of Pártay *et al.* defines the set of truly interfacial molecules as

the ones "seen" from the opposite phase.[14] The procedure can be visualized as moving a probe sphere, starting from the bulk opposite phase, along test lines perpendicular to the macroscopic plane of the interface. Once the probe sphere touches the first molecule of the phase of interest, it is stopped and the touched molecule is marked as being interfacial. Finally, several methods that are even free from the assumption that the interface is macroscopically planar have also been proposed in the past decade.[15–17]

After the real, capillary wave corrugated surface of a fluid phase has been located, the profile of various thermodynamic quantities, such as the density[8,18] energy, pressure, or solvation free energy of a given molecule,[19] can be calculated as a function of the position relative to the intrinsic interface. The determination of this intrinsic profile of various quantities can be of great help in understanding surface thermodynamics, as it provides the change of the corresponding quantity with the distance from the interface up to its convergence to the bulk phase value. For example, the intrinsic analysis has been essential to the investigation of surface properties of ionic liquids,[20–23] explanation of the surface tension anomaly of water,[24,25] immersion depth of surfactants in water,[26] oil-water interfaces,[27] structure of ionic aqueous solutions and their intrinsic interfacial potential,[28] the plausibility of the "HCN World" hypothesis,[29] as well as the adhesive properties of Newton black films.[30]

Besides the exact location of the intrinsic surface itself, these methods provide in addition the full list of surface molecules. Thus, by removing the molecules constituting the surface layer and repeating the whole procedure, the molecules of the second layer beneath the surface can also be identified. This process can be repeated until the physical meaning of the concept of molecular layers beneath the surface is completely lost.[14] This detection of the consecutive subsurface layers allows for an alternative way of describing surface thermodynamics, in which the quantity of interest is averaged over each layer. Hence, its change from one layer to the other can be followed. Similarly to the calculation of the intrinsic profiles, this layer-by-layer approach also describes the change of the thermodynamic quantities upon getting farther from the interface.

In this paper, we show how it is possible to gather information on the contribution of each subsequent layer to several thermodynamic quantities (layer-by-layer analysis), both simply as a function of the position along the normal axis in the global reference frame, and as a function of the displacement from the local position of the interface. As a prototype of a soft interface, we take the liquid/vapor interface of a Lennard-Jones fluid well below the critical point, where the concept of a continuous, quasi two-dimensional interface can be applied.

II. COMPUTATIONAL DETAILS

The subject of our investigation is the liquid/vapor interface of a Lennard-Jones liquid as a general model of a soft interface. For the sake of definiteness, we report physical units that correspond to liquid argon.[31] We performed molecular dynamics simulations in the canonical ensemble at 80 K, modelling atoms using the Lennard-Jones potential $U(r) = 4\epsilon$ $[(\sigma/r)^{12} - (\sigma/r)^{6}]$, with $\sigma = 0.34$ nm and $\epsilon = 0.998$ kJ/mol (corresponding to 120 K, so that the reduced temperature

$T^* = T/\epsilon = 2/3$). This temperature is close to the triple point of the Lennard-Jones fluid,[32–35] so, in order to check that the high-density region of the system is indeed in the liquid state, we performed the calculation of the probability distribution of the averaged $\bar{q}_6$ bond order parameter,[36] for equilibrated configurations of the liquid/vapor interface, which resulted in an unimodal distribution peaked at $\bar{q}_6 = 0.085$, and no atom having $\bar{q}_6 > 0.25$, confirming the absence of crystal-like structures.

The length of the rectangular simulation cell edges was 4 nm along the x and y directions and 18 nm along the macroscopic surface normal $\hat{z}$. Periodic boundary conditions were applied. We simulated in total 2237 atoms, integrating the equations of motion every 1 fs and keeping the average temperature constant using the algorithm of Nosé and Hoover[37,38] with a relaxation constant of 0.1 ps. A simple cutoff at 1 nm was applied to the Lennard-Jones interaction, and long-range corrections were not employed. Simulation was performed with an in-house modified version of the GROMACS simulation package[39,40] version 5, which allows to save the pressure contributions, as described later, to the trajectory files along with positions, velocities, and forces.

To simulate the liquid/vapor interface, we filled a region, about 7 nm wide along $\hat{z}$ and the size of the box edges along the other two directions, with copies of a smaller, equilibrated simulation box of argon in the liquid state. As a result, in each of the periodic cells, two liquid/vapor planar interfaces are present, as shown in Fig. 1. Periodic boundary conditions prevent the formation of a single, spherical interface.

The system was equilibrated for 1 ns, during which the potential energy and the components of the stress tensor relaxed to their equilibrium values. During a run of 10 ns, we saved particle positions and pressure contributions every 100 ps for off-line analysis. We used the ITIM algorithm[14] in its implementation for the GROMACS simulation code[17] using a probe sphere radius of 0.17 nm (corresponding to the atomic radius $\sigma/2$) to identify surface atoms. We excluded from the surface analysis the atoms belonging to the vapor phase by using a cutoff based cluster search.[41] The cutoff distance for the cluster search was set to 0.5 nm, which corresponds to the first minimum in the radial distribution function. Thanks to the cluster search, the method can be applied up to fairly high temperatures (for example, it was applied up to 85% of the critical temperature of water[24]), provided that the second-largest cluster in the system is considerably smaller than the largest one. Close to the critical point, this approach
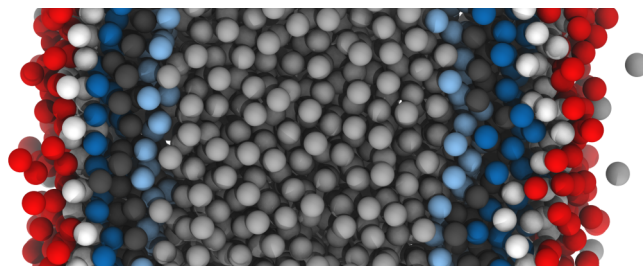

FIG. 1. Detail of a simulation snapshot of the liquid/vapor interface of a Lennard-Jones fluid at reduced temperature $T^* = 2/3$. The atoms of the first 5 layers are highlighted in different colours (red, white, blue, dark gray, light blue). Some atoms in the vapor phase close to the interface are visible on the right.
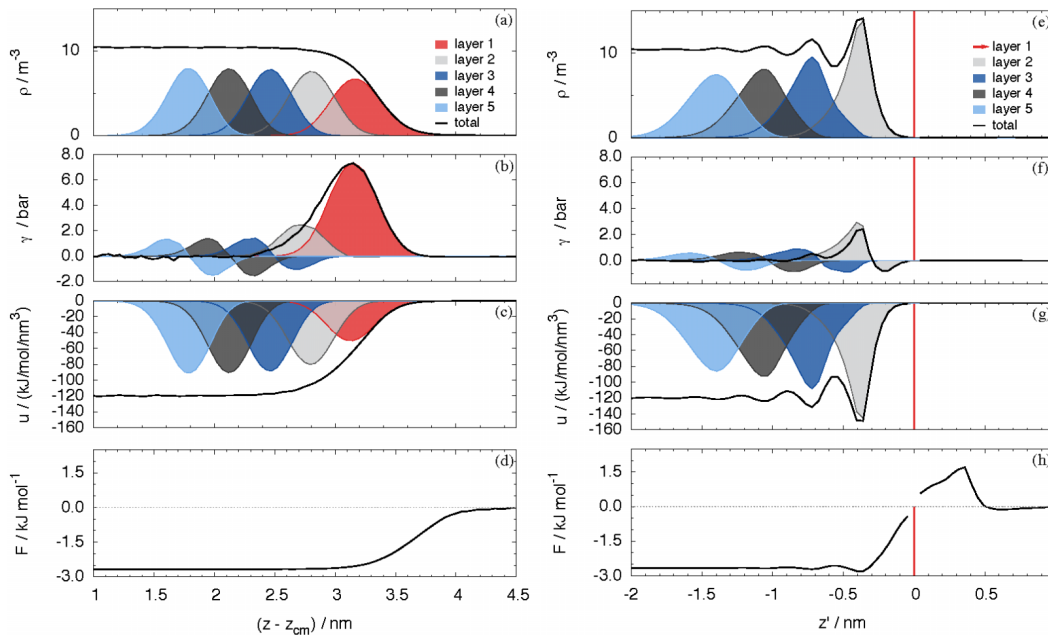
FIG. 2. Non-intrinsic (left) and intrinsic (right) profiles: number density (a)-(e); surface tension (b)-(f); energy density (c), (g); and Helmholtz free energy (d), (h). The contribution of the first layers is also reported. In the intrinsic profiles, the Dirac delta contribution of the first layer has been removed, and the position of the interface is marked by a vertical line. The profiles are normalized in the following way: $\int \rho(z)dV = N$, $\int \gamma(z)dz = \gamma$, and $\int u(z)dV = U$. The free energy profile defined such that $F(b) - F(a)$ is the reversible work needed to bring a particle from position a to position b.

is not applicable any more, because the cluster algorithm fails in identifying the liquid phase, and because the strong fluctuations of the interface go beyond the quasi-planar approximation. In this case, more sophisticated methods such as the generalized ITIM[17] can be used, although too close to the critical point, the concept of a single, macroscopic interface ceases to exist.

By repeatedly applying the algorithm, we first identified the interfacial layers of the two liquid/vapor interfaces and then proceeded to associate atoms to successive layers, as depicted in Fig. 1. To determine the position of the intrinsic interface at any (x, y) point, a triangular interpolation scheme was used.[18]

III. LOCAL NUMBER DENSITY

We denote with $\mathcal{Z}$ the configurational integral of the system,

$$\mathcal{Z} = \int e^{-\beta U} d\Gamma, \tag{1}$$

where U is the potential part of the Hamiltonian, $\beta = 1/(k_B T)$ is the inverse thermal energy, and the integration is performed over all $3N$ configurational degrees of freedom, which in this case are simply the positions of the particles, $\Gamma = (\mathbf{r}_1, \mathbf{r}_2, \ldots, \mathbf{r}_N)$. The canonical average of a generic quantity B can be written as $\langle B \rangle = \mathcal{Z}^{-1} \int B e^{-\beta U} d\Gamma$.

The density is a local quantity and there is no ambiguity in the definition of a position-dependent, local expression. The non-intrinsic number density profile is simply defined as

$$\rho(z) = \frac{1}{A} \left\langle \sum_i^N \delta(z - z_i) \right\rangle, \tag{2}$$

where A is the cross-sectional area of the simulation box orthogonal to the surface normal. The total number of particles

in the simulation box is then $N = \int \rho(z)dV$. As with other non-intrinsic profiles, we position the reference frame at the location of the instantaneous center of mass of the system, with the liquid phase shifted so that it does not cross the periodic boundary conditions. After applying repeatedly the ITIM analysis to determine the atoms belonging to the first 7 layers, the layer-by-layer density profile of one layer is simply computed by restricting the sum of Eq. (2) to the atoms belonging to the layer of interest. Note that this analysis cannot be performed for an arbitrary number of layers, as close to the middle of the liquid phase, due to fluctuations, the layers will not be covering the complete surface and, therefore, the ITIM analysis will fail. In the present case, the width of the liquid slab is large enough, as it will be shown, to guarantee convergence of all quantities to their bulk values before the ITIM analysis stops being applicable.
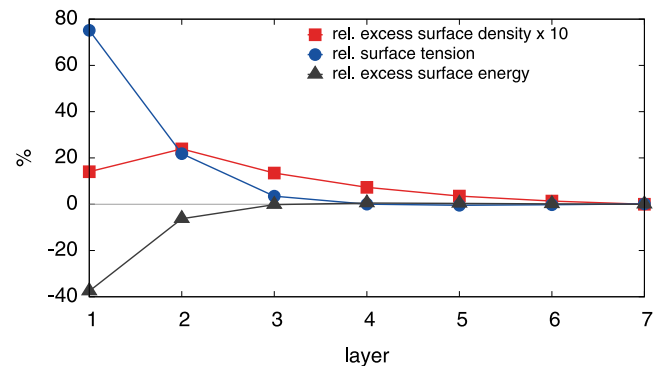

FIG. 3. Layer dependence of several quantities: relative surface excess number density $\rho_s^{(l)}/\rho_{liq}$ (squares, scaled by a factor 10); relative surface excess energy density $u_s^{(l)}/u_{liq}$ (triangles) and surface tension contribution $\gamma^{(l)}$ (circles).

The intrinsic density profile can be written as

$$\rho_I(z') = \frac{1}{A}\left\langle \sum_i^N \delta\left(z' - z_i + \xi(x_i, y_i)\right)\right\rangle, \quad (3)$$

where $\xi(x_i, y_i)$ is the location of the interface along $\hat{z}$ in correspondence of the projected position of the particle on the surface itself, and where the displacement from the instantaneous surface is denoted by z', to avoid confusion with the position in the simulation box reference frame, z. The intrinsic density profile can be, in turn, decomposed into the contribution coming from different layers, similarly to the non-intrinsic density profile. By construction, the density profile will always present a delta-like contribution at $z' = 0$, as by definition, surface molecules are at zero distance from the surface. This also means that the intrinsic contribution of the first layer will be just a delta function. From the density profile, it is trivial to obtain the profile of the kinetic energy density, $K(z)$ $= 1/A\left\langle \sum_i^N (m/2)v_i^2\delta(z - z_i)\right\rangle = (3/2)k_BT\rho(z)$, or, equivalently, the (constant) temperature profile $T(z) = (2/3)K(z)/\rho(z)$.

The results for the number density profile are reported in Figs. 2(a) and 2(e). Because of the presence of thermal capillary waves, each layer in the non-intrinsic density profile, Fig. 2(a), is characterized by a Gaussian distribution, with a fairly uniform distribution of particles across the different layers. Although the non-intrinsic distribution of particles in the first layer has a larger width than in the subsequent ones, its height is smaller. In fact, the surface density in the first three layers is about 2% higher than in the inner layers, as shown in Fig. 3, where we report the relative surface excess density of the first 7 layers. The surface excess density of layer l is defined as $\rho_s^{(l)} = \rho_{\text{liq}}\left(N^{(l)}/N^{(\text{liq})} - 1\right)$, where $N^{(l)}$ is the average number of atoms in layer l, and where the 7-th layer has proven to be deep enough to be considered representative of the bulk, $N^{(7)} \simeq N^{(\text{liq})}$, as it guarantees convergence of all inspected quantities within less than 0.5%. With this definition, the surface excess density can be expressed as $\rho_s = \sum_l \rho_s^{(l)}$, and in this approach, it is an independent quantity, since it is not used to define implicitly the location of the dividing surface.

The intrinsic density profile is reported in Fig. 2(e), where the distribution of the first layer is, by construction, a delta function at the origin of the intrinsic coordinate frame, and subsequent layers contribute in creating a well structured profile, in which at least three correlation peaks can be clearly identified. Interestingly, the intrinsic distributions of the layers do not have a Gaussian shape. The second layer is more narrowly distributed than a Gaussian and is not symmetric, this feature being partly shared by the third and fourth layers. This behaviour originates most probably from the packing of atoms close to the surface, a feature that is completely lost in the non-intrinsic density profile due to the smearing caused by capillary waves.

IV. ENERGY DENSITY

The second quantity that we consider here is the energy density, which is a non-local quantity. Even for pair interactions, like the Lennard-Jones potential, there is no obvious prescription on how to distribute in space the energy associated to each pair,[42] even though it is customary to associate half of it to each of the particles composing the pair. In this way, one can write the energy density profile as

$$u(z) = \frac{1}{A}\left\langle \sum_i^N \sum_{j\neq i}^N \frac{U_{ij}}{2}\delta(z - z_i)\right\rangle, \quad (4)$$

where U_{ij} is the energy of the ij pair. This represents the energy content per unit volume associated to the slab at position z. The contribution of layer l, $U^{(l)}$ to the total energy can be calculated similarly to the density case, $\rho^{(l)}$, and the intrinsic energy density profile takes the form

$$u_I(z') = \frac{1}{A}\left\langle \sum_i^N \sum_{j\neq i}^N \frac{U_{ij}}{2}\delta(z' - z_i + \xi(x_i, y_i))\right\rangle. \quad (5)$$

The energy density profile is qualitatively similar to the density profile, for both the non-intrinsic (Fig. 2(c)) and intrinsic (Fig. 2(g)) cases, with a somewhat larger difference between the first layer distribution and the subsequent ones, the surface layer having a less negative energy, (by about 40%) as shown in Fig. 3. The layer surface excess energy $u_s^{(l)}$ is defined along the lines of the surface excess density, using the average energy in the layer and the energy density in the liquid phase instead of $N^{(l)}$ and ρ_{liq}, respectively.

To understand in more depth the relationship between the number and energy density profile, it is instructive to look at the profile of the energy per particle, defined as the ratio of energy and number density $u(z)/\rho(z)$ for the non-intrinsic profile and $u_I(z)/\rho_I(z)$ for the intrinsic profile. The result is, at first sight, surprising, as the two curves, shown in Fig. 4, can be superimposed almost perfectly, once the origin of the coordinate system is adjusted. The reason for this similarity has to be sought in the non-local nature of the energy, which is the sum of each pair contribution within the cutoff radius. In this sense, local inhomogeneities are smeared out, and, as long as the amplitude of the capillary waves is smaller than the interaction radius, one could expect the intrinsic and non-intrinsic profiles of the energy per particle to be very similar (as we will show later, this is not the case for the Helmholtz free energy). A simple geometrical model along the lines of Dupré[42,43] can be used to understand to what extent the non-local nature of the energy is smearing the profile. One can assume, as a crude approximation, a sharp intrinsic density profile, such that $\rho_I(z') = \rho_{\text{vap}}$ for $z' > 0$ and $\rho_I(z') = \rho_{\text{liq}}$ for $z' < 0$. If $u_{\text{liq}}/\rho_{\text{liq}}$ is the energy per particle in the liquid phase far from the interface, $u_{\text{vap}} \simeq 0$, and R is an effective interaction radius in which this energy is concentrated, then, once a particle comes closer than a distance R to the interface, its energy will become proportional to the volume of the spherical cap still in the liquid region, $z < 0$, so that $u(z) \propto u_{\text{liq}}\pi z^2(R - z/3)$. This function is shown in Fig. 4 as a dotted line where the effective radius has been determined to be $R = 0.9$ nm by a Marquardt–Levenberg least-square fit to the non-intrinsic profile. The almost perfect match between this model result and the non-intrinsic profile $u(z)/\rho(z)$ seems at first sight to show that the non-local nature of the energy is smearing out the inhomogeneities to yield a profile that is indistinguishable from that generated by a step-like profile of a continuum fluid. However, the comparison with the intrinsic
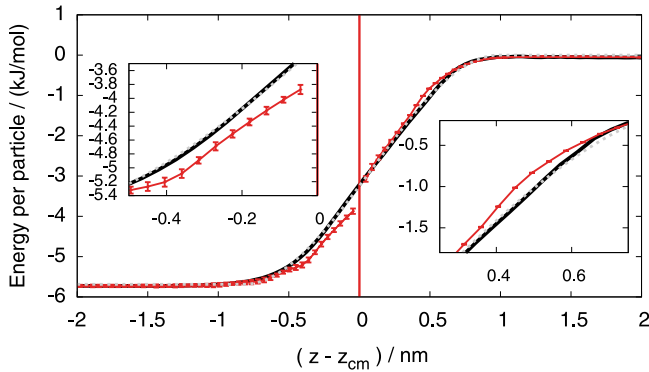
FIG. 4. Energy per particle, non-intrinsic ($u(z)/\rho(z)$, solid line), and intrinsic ($u_I(z')/\rho_I(z')$, solid line with error bars). The dotted line is the result of the fit to the simple geometrical model described in the text. The insets show details of the curve in the region right before and right after the interface location ($z = 0$).

profile $u_I(z')/\rho_I(z')$ shows that there are indeed some local features that the model cannot reproduce, as highlighted in the insets of Fig. 4. Even though the intrinsic profile suffers from larger statistical noise with respect to the non-intrinsic one, originating from the large oscillations present in both the denominator and numerator, the difference between the two curves is larger than the indetermination. This suggests that it is actually the combination of the smearing effects, due to both the non-locality of the energy and the capillary waves, that makes the simple model match so well with the non-intrinsic profile.

V. HELMHOLTZ FREE ENERGY AND ENTROPY

We continue our analysis with the profiles of global thermodynamic quantities. Thermodynamical quantities, such as the (excess) energy U and Helmholtz free energy F, can be computed, as usual, as $U = -\partial \log \mathcal{Z}/\partial \beta$ and $F = -k_B T \log (\mathcal{Z}/V^N)$. To introduce the position-dependent equivalent of these two quantities, it is customary to define $\mathcal{Z}(z)$ as the configurational integral under the condition that one particle (say, the first) is at position $z_1 = z$, thus, $\mathcal{Z}(z) = \int e^{-\beta U} \delta(z - z_1)d\Gamma$. Since particles can be exchanged without changing the configurational integral, this allows us to write

$$\mathcal{Z}(z) = \frac{1}{N} \int e^{-\beta U} \sum_i \delta(z - z_i)d\Gamma. \tag{6}$$

The non-intrinsic number density profile, Eq. (2), can be thus expressed in terms of $\mathcal{Z}(z)$ as

$$\rho(z) = (N/A)\mathcal{Z}(z)/\mathcal{Z}. \tag{7}$$

Similarly, the Helmholtz free energy profile can be evaluated, up to an immaterial constant, as

$$F(z) = -k_B T \log \rho(z). \tag{8}$$

The free energy difference $F(a) - F(b)$ represents the (reversible) work needed to move one of the particles from position b to position a, letting all others free to rearrange.

The excess energy profile

$$U(z) = -\frac{\partial \log \mathcal{Z}(z)}{\partial \beta} = \frac{\int e^{-\beta U} U \sum_i \delta(z - z_i)d\Gamma}{N\mathcal{Z}(z)} \tag{9}$$

can be expressed in terms of canonical averages, using Eq. (7), as

$$U(z) = \frac{1}{\rho(z)} \left\langle \frac{U}{A} \sum_i^N \delta(z - z_i) \right\rangle. \tag{10}$$

This, we would like to stress, is the total excess energy of the system, under the condition that one of the particles is located at position z along the normal axis, *not* the energy density profile $u(z)$ discussed previously. In the thermodynamic limit, the total energy U is uncorrelated with the z position of its particles, so that $\langle U \sum_i^N \delta(z - z_i) \rangle = \langle U \rangle \langle \sum_i^N \delta(z - z_i) \rangle$. Another way to see this is to consider the conditional average value of the energy $\langle U\delta(z - z_1) \rangle / \langle \delta(z - z_1) \rangle$, and noticing that if the system is infinite, it is always possible to find a particle at position z and to exchange it with particle 1 in previous expression, so that all configurations contribute to the average, effectively removing the condition. Either ways, the result is that $U(z) = \langle U \rangle$. We checked explicitly that the total energy profile, Eq. (10), is indeed constant, as it can be seen from Fig. 5, where we report the ratio $U(z)/\langle U \rangle$ and the number density profile, to show the location of the two phases. The reduced sampling in the gas phase is at the origin of the larger fluctuations in the energy data, which can be observed in the region $|z| > 4$ nm.

A constant energy profile implies that the changes in excess free energy $F(z) = U(z) - TS(z)$ are of purely entropic origin. The reason for this is that when "pinning" a particle at a given position z, the average total potential energy is not changed (as long as all other particles are free to sample the configurational space), while one degree of freedom has been blocked: this influences the total entropy of the system. If a particle is pinned in the gas phase, a larger amount of entropy will be subtracted from the system, in comparison to it being pinned in the liquid phase, simply because of the different volumes accessible in the two phases. As a result, the entropy of the system $S(z)$ will be larger when constraining a particle to be in the liquid region than in the gas one.

The free energy profile has the inconvenience of not being separable in a meaningful way into the contributions of the components of the system, such as the different
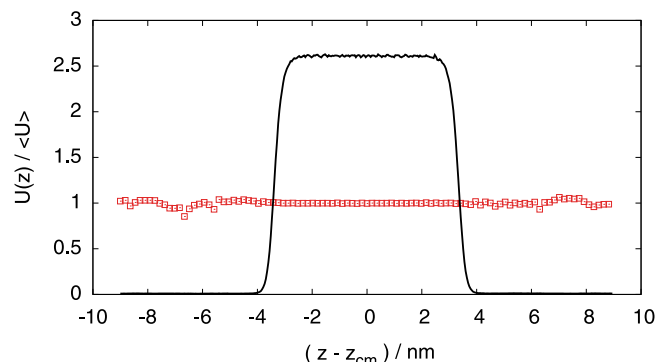

FIG. 5. Ratio of the total energy profile $U(z)$ to the average total energy $\langle U \rangle$. The density profile (arbitrary units) is also shown for reference.

layers, due to its intrinsic nonlinearity. Nevertheless, it is still possible to calculate the intrinsic free energy profile as $F_I(z') = -k_B T \log(\rho_I(z'))$.

The obtained intrinsic free energy profile (Fig. 2(h)) shows some additional features relative to the non-intrinsic one (Fig. 2(d)), consistently with previous works.[28] Evidently, the two profiles converge to the same values in the two bulk phases, leaving the roughly 3 kJ/mol ($\simeq 4.5RT$, where R is the gas constant) free energy difference between the two phases unchanged. However, the intrinsic free energy profile exhibits noticeable oscillations at the liquid side of the interface, around $z \simeq -0.5$ nm. More importantly, it exhibits a clear maximum at the vapor side of the interface, at $z \simeq 0.3$ nm. This distance corresponds roughly to one atomic diameter. This finding is certainly related to our definition of the liquid phase through the cluster analysis (i.e., an atom that is closer than 0.5 nm to a liquid phase atom is also regarded to be part of the liquid phase). Nevertheless, the presence of this maximum still suggests that the transfer of the atoms from the vapor to the liquid phase might well be an activated process, with a small activation barrier, the height of which is comparable with RT.

VI. LOCAL PRESSURE AND SURFACE TENSION

The study of stress distribution across the interfacial regions of non-homogeneous fluids has seen a renewed interest in recent years. The earlier studies in liquid/vapor interfaces[44] have laid the foundation of a practice that is now applied to various complex liquids including lipid bilayers, vesicles, and micelles.[45–48] While some momenta of the stress tensor distribution are uniquely defined (for example, in planar interfaces, the normal stress and the surface tension), this is not true in general for the local stress tensor itself, which can be defined, up to a divergence-free second rank tensor, in a path-dependent form. For pairwise additive potentials $U(\mathbf{r}_{ij})$, for which the force is $f^\alpha(\mathbf{r}_{ij}) = -\nabla^\alpha U(\mathbf{r}_{ij})$, the configurational part σ_c of the local stress tensor σ has the form $\sigma_c^{\alpha\beta}(\mathbf{r}) = -1/2 \left\langle \sum'_{ij} f^\alpha_{ij} \int_{C_{ij}} ds^\beta \delta(\mathbf{r}-\mathbf{s}) \right\rangle$, where the primed sum is performed over all particle indices i and $j \neq i$ and the integration contour is an open path C_{ij} connecting particles i and j. With the trivial ideal gas contribution, the complete stress tensor can be written as $\sigma^{\alpha\beta}(\mathbf{r}) = \sigma_c^{\alpha\beta}(\mathbf{r}) - \left\langle \sum_i^N m v_i^\alpha v_i^\beta \delta(\mathbf{r}-\mathbf{r}_i) \right\rangle$.

As a consequence of this freedom, quantities based on the local stress tensor are, in general, not uniquely defined. However, different choices for the integration contour, such as the Irving-Kirkwood[49] and the Harasima[50] ones, have been shown to yield comparable surface tension profiles.[51] The notion of a local surface tension density $\gamma(\mathbf{r}) = \sigma_T(\mathbf{r}) - \sigma_N$, here expressed as a function of the tangential and normal local stress components σ_T and σ_N, respectively, although not being well defined on the microscopical level, can still represent an important guidance in the interpretation of atomistic computer simulation results and in understanding the microscopic picture of surface thermodynamics (Fig. 6).

A particularly interesting feature of the Harasima contour for planar interfaces is that in the tangential part of the stress tensor, the explicit dependence on a path disappears, and the contribution from a pair of particles to the total
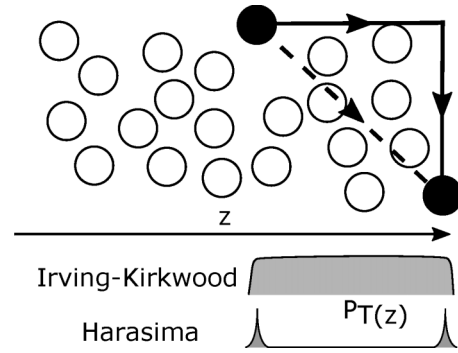

FIG. 6. Schematic representation of the Irwing–Kirkwood (dashed line) and Harasima (solid line) paths for the calculation of the pressure profile.

stress tensor is equally distributed at the positions z_i and z_j of the particles along the interface normal, namely, $\sigma_c^{\alpha\alpha}(z) = -1/(2A)\left\langle \sum'_{ij} f^\alpha_{ij} r^\alpha_{ij} \delta(z-z_i) \right\rangle$, for $\alpha = x, y$. In this sense, it is possible to associate to each particle its contribution to the tangential part of the stress tensor, writing

$$\sigma_{c,i}^{\alpha\alpha} = -1/2 \sum_{j\neq i}^N f^\alpha_{ij} r^\alpha_{ij} \quad (\alpha = x, y), \tag{11}$$

where the normalization has been chosen such that the diagonal part of the stress tensor, $\sigma_c^{\alpha\alpha}$, is the sum over all particle contributions, divided by the volume $\sigma_c^{\alpha\alpha} = \sum_i^N \sigma_{c,i}^{\alpha\alpha}/V$. Note that the expression for the normal component ($\alpha = z$), equivalent to Eq. (11) will not yield the correct normal stress, as it does not correspond to any physical integration contour.[44] At equilibrium, this is a minor drawback, since the normal component of the total stress tensor (kinetic plus configurational contribution) has to be constant to ensure mechanical stability, and as a consequence also the intrinsic profile of the normal component would just be a constant. This is true not only at the macroscopic or mesoscopic level[52] but also at the microscopic one.[53]

The simple fact that Eq. (11) associates to each particle a contribution to the tangential stress has important implications. The first consequence is of practical relevance because it makes possible, during a run, to store the pressure tensor contribution associated to each particle for offline analysis, just like positions, velocities, or forces, thus avoiding time-consuming and memory-intensive sampling of the stress tensor on three-dimensional grids (which consists usually of more points than particles in the simulation). The second consequence is that this representation allows for a straightforward implementation of both the layer-by-layer and intrinsic analysis of the surface tension. The non-intrinsic surface tension profile can then be written as

$$\gamma(z) = \frac{1}{A}\left\langle \sum_i^N \frac{\sigma_i^{xx}+\sigma_i^{yy}}{2}\delta(z-z_i) \right\rangle - \sigma^{zz}, \tag{12}$$

so that the total surface tension $\gamma = \int \gamma(z)dz$. The intrinsic surface tension profile is the obvious extension

$$\gamma_I(z') = \frac{1}{A}\left\langle \sum_i^N \frac{\sigma_i^{xx}+\sigma_i^{yy}}{2}\delta(z'-z_i+\xi(x_i,y_i)) \right\rangle - \sigma^{zz}. \tag{13}$$

We would like to stress that this decomposition into particle contribution would not be possible with the Irving-Kirkwood path. This does not prevent in principle to compute an intrinsic pressure profile using the latter path, but the analysis would be considerably more complicated.

The non-intrinsic and intrinsic profiles of the surface tension are shown in Figs. 2(b) and 2(f), respectively. The contribution to the surface tension profile, instead of just decreasing when passing to the inner layers, acquires also a characteristic antisymmetric profile. While, on average, the inner layers contribute very little to the overall surface tension, depending on the displacement from the average position, the contribution can be positive (inwards with respect to the average position) or negative (for locations closer to the interface). From the intrinsic profile, one can estimate the properties of the region where the contribution to the surface tension is concentrated. This region is about 1 nm wide and shows a considerable structure of the profile to which the first two layers are contributing. Surprisingly, the surface tension profile shows a negative tension region right below the first layer. Looking at the contribution from the different layers, $\gamma^{(l)}$, reported in Fig. 3, it is possible to appreciate that about 80% of the contribution to the total surface tension comes indeed from the first layer, while the second one contributes for the remaining 20%. Successive layers are not contributing appreciably to the surface tension of the system.

VII. CONCLUSIONS

The intrinsic analysis can provide a privileged point of view on the properties of soft interfaces by removing the smearing effect of thermal capillary wave and revealing the local details of the interface. Here, we introduced, along the lines of the intrinsic density profile, the intrinsic counterparts of energy density, surface tension, and Helmholtz free energy and applied them to the problem of a model soft interface. Several results of the analysis were unexpected. First of all, the strong order observed in the intrinsic density profile, which is also seen in the intrinsic energy density profile, disappears when considering the intrinsic energy density profile per particle, which is very close to its non-intrinsic counterpart. Moreover, to an extremely good approximation, both the intrinsic and non-intrinsic profiles of the energy density per particle are proportional to the average amount of liquid within an effective interaction radius. Even though this fact is a bit surprising, given the strong density fluctuation in the intrinsic density profile, its origins are rooted in the non-local nature of the energy.

In the second place, the contribution from the different molecular layers to the surface tension vanished, not surprisingly, after the second layer. However, the contribution of layers deeper than the second one is zero on average but shows a characteristic antisymmetric distribution, whose traces are still present in the second and third layers, creating a region of negative surface tension right before the surface.

One last remark about an important feature of the intrinsic analysis is due: the location of the interface and the density profile are not, at least directly, dependent on each other. This allows us to bypass the difficulties inherent to the canonical approach, which uses the excess surface density to define the location of the interface (or viceversa), making the estimate of the former quantity somewhat arbitrary. With the intrinsic analysis of surface molecules, most of this arbitrariness is removed, the only free parameter being the probe sphere radius, although there is a physically meaningful range even for it.[13] Thus, it becomes possible to make precise estimates of surface excess quantities like density, energy density, or surface tension, as we have reported here. Further, layer-by-layer and intrinsic analysis investigations of various molecular liquids including dipolar and hydrogen bonding ones are currently in progress.

[1]J. Penfold, Curr. Opin. Colloid Interface Sci. **7**, 139 (2002).
[2]M. Tolan, *X-Ray Scattering from Soft-matter Thin Films* (Springer, Berlin, 1999).
[3]F. Jähnig, Proc. Natl. Acad. Sci. U. S. A. **76**, 6361 (1979).
[4]A. J. Cross and G. R. Fleming, Biophys. J. **46**, 45 (1984).
[5]Y. Shen, Nature **337**, 519 (1989).
[6]G. L. Richmond, Chem. Rev. **102**, 2693 (2002).
[7]M. P. Allen and D. J. Tildesley, *Computer Simulation of Liquids* (Oxford University Press, Oxford, 1989).
[8]E. Chacón and P. Tarazona, Phys. Rev. Lett. **91**, 166103 (2003).
[9]P. Linse, J. Chem. Phys. **86**, 4177 (1987).
[10]I. Benjamin, J. Chem. Phys. **97**, 1432 (1992).
[11]M. Jorge and M. N. D. S. Cordeiro, J. Phys. Chem. C **111**, 17612 (2007).
[12]J. Chowdhary and B. M. Ladanyi, J. Phys. Chem. B **110**, 15442 (2006).
[13]M. Jorge, P. Jedlovszky, and M. N. D. S. Cordeiro, J. Phys. Chem. C **114**, 11169 (2010).
[14]L. B. Pártay, G. Hantal, P. Jedlovszky, Á. Vincze, and G. Horvai, J. Comput. Chem. **29**, 945 (2008).
[15]M. Mezei, J. Mol. Graphics Modell. **21**, 463 (2003).
[16]A. P. Willard and D. Chandler, J. Phys. Chem. B **114**, 1954 (2010).
[17]M. Sega, S. S. Kantorovich, P. Jedlovszky, and M. Jorge, J. Chem. Phys. **138**, 044110 (2013).
[18]M. Jorge, G. Hantal, P. Jedlovszky, and M. N. D. S. Cordeiro, J. Phys. Chem. C **114**, 18656 (2010).
[19]M. Darvas, M. Jorge, M. N. D. S. Cordeiro, S. S. Kantorovich, M. Sega, and P. Jedlovszky, J. Phys. Chem. B **117**, 16148 (2013).
[20]Z. P. M. Lísal and P. Izák, Phys. Chem. Chem. Phys. **14**, 5164 (2012).
[21]G. Hantal, M. N. D. S. Cordeiro, and M. Jorge, Phys. Chem. Chem. Phys. **10**, 21230 (2011).
[22]M. Lísal and P. Izák, J. Chem. Phys. **139**, 014704 (2013).
[23]M. N. D. S. C. G. Hantal, I. Voroshylova, and M. Jorge, Phys. Chem. Chem. Phys. **14**, 5200 (2012).
[24]M. Sega, G. Horvai, and P. Jedlovszky, Langmuir **30**, 2969 (2014).
[25]M. Sega, G. Horvai, and P. Jedlovszky, J. Chem. Phys. **141**, 054707 (2014).

[26]N. Abrankó-Rideg, M. Darvasa, G. Horvai, and P. Jedlovszky, J. Phys. Chem. B **117**, 8733 (2013).

[27]F. Bresme, E. Chacón, P. Tarazona, and K. Tay, Phys. Rev. Lett. **101**, 056102 (2008).

[28]F. Bresme, E. Chacón, P. Tarazona, and A. Wynveen, J. Chem. Phys. **137**, 114706 (2012).

[29]B. Fábián, M. Szőri, and P. Jedlovszky, J. Phys. Chem. C **118**, 21469 (2014).

[30]F. Bresme, E. Chacón, H. Martínez, and P. Tarazona, J. Chem. Phys. **134**, 214701 (2011).

[31]A. Rahman, Phys. Rev. **136**, A405 (1964).

[32]J.-P. Hansen and L. Verlet, Phys. Rev. **184**, 151 (1969).

[33]A. Ladd and L. Woodcock, Mol. Phys. **36**, 611 (1978).

[34]J. K. Johnson, J. A. Zollweg, and K. E. Gubbins, Mol. Phys. **78**, 591 (1993).

[35]A. Ahmed and R. J. Sadus, J. Chem. Phys. **131**, 174504 (2009).

[36]W. Lechner and C. Dellago, J. Chem. Phys. **129**, 114707 (2008).

[37]S. Nosé, Mol. Phys. **52**, 255 (1984).

[38]W. Hoover, Phys. Rev. A **31**, 1695 (1985).

[39]H. J. Berendsen, D. van der Spoel, and R. van Drunen, Comput. Phys. Commut. **91**, 43 (1995).

[40]S. Páll, M. Abraham, C. Kutzner, B. Hess, and E. Lindahl, "Tackling exascale software challenges in molecular dynamics simulations with GROMACS," in *Solving Software Challenges for Exascale*, Lecture Notes in Computer Science Vol. 8759, edited by S. Markidis and E. Laure (Springer International Publishing, 2015).

[41]L. B. Partay, G. Horvai, and P. Jedlovszky, J. Phys. Chem. C **114**, 21681 (2010).

[42]J. S. Rowlinson and B. Widom, *Molecular Theory of Capillarity* (Dover Publications, Inc., Mineola, New York, 1982).

[43]A. Dupré and P. Dupré, *Théorie Mécanique de la Chaleur* (Gauthier-Villars, Paris, 1869).

[44]P. Schofield and J. Henderson, Proc. R. Soc. A **379**, 231 (1982).

[45]J. Gullingsrud and K. Schulten, Biophys. J. **86**, 3496 (2004).

[46]O. S. Ollila, H. J. Risselada, M. Louhivuori, E. Lindahl, I. Vattulainen, and S. J. Marrink, Phys. Rev. Lett. **102**, 078101 (2009).

[47]S. Ollila, M. T. Hyvönen, and I. Vattulainen, J. Phys. Chem. B **111**, 3139 (2007).

[48]P. S. Niemelä, S. Ollila, M. T. Hyvönen, M. Karttunen, and I. Vattulainen, PLoS Comput. Biol. **3**, e34 (2007).

[49]J. Irving and J. G. Kirkwood, J. Chem. Phys. **18**, 817 (1950).

[50]A. Harasima, Adv. Chem. Phys. **1**, 203 (1958).

[51]J. Sonne, F. Y. Hansen, and G. H. Peters, J. Chem. Phys. **122**, 124903 (2005).

[52]M. Sbragaglia and D. Belardinelli, Phys. Rev. E **88**, 013306 (2013).

[53]K. S. Cheung and S. Yip, J. Appl. Phys. **70**, 5688 (1991).